26. Z. H. Xiong, D. Wu, Z. V. Vardeny, J. Shi, *Nature* **427**, 821–824 (2004).
27. C. W. Tang, *Appl. Phys. Lett.* **48**, 183–185 (1986).
28. C. M. Ramsdale *et al.*, *J. Appl. Phys.* **92**, 4266–4270 (2002).
29. K. Vandewal, K. Tvingstedt, A. Gadisa, O. Inganäs, J. V. Manca, *Nat. Mater.* **8**, 904–909 (2009).
30. A. J. Heeger, *Adv. Mater.* **26**, 10–27 (2014).
31. P. A. Bobbert, W. Wagemans, F. W. van Oost, B. Koopmans, M. Wohlgenannt, *Phys. Rev. Lett.* **102**, 156604 (2009).
32. Z. G. Yu, *Nat. Commun.* **5**, 4842 (2014).

ACKNOWLEDGMENTS

The authors acknowledge financial support from the Ministry of Science and Technology of China (grants 2016YFA0200700 and 2017YFA0206600); the European Union 7th Framework Programme under the Marie Curie Actions (256470-ITAMOSCINOM), the European Research Council (257654-SPINTROS), and the NMP project (263104-HINTS); the Spanish Ministry of Economy (project no. MAT2015-65159-R); the Basque Government (project no. PRE_2016_2_0025); the National Natural Science Foundation of China (grant 21673059); and the CAS Pioneer Hundred Talents Program. All data are reported in the main paper and supplementary materials.

SUPPLEMENTARY MATERIALS

www.sciencemag.org/content/357/6352/677/suppl/DC1
Materials and Methods
Figs. S1 to S4
Reference (*33*)

27 April 2017; accepted 12 July 2017
10.1126/science.aan5348

STELLAR ASTROPHYSICS

An unusual white dwarf star may be a surviving remnant of a subluminous Type Ia supernova

S. Vennes,[1]* P. Nemeth,[2,3] A. Kawka,[1] J. R. Thorstensen,[4] V. Khalack,[5] L. Ferrario,[6] E. H. Alper[4]

Subluminous Type Ia supernovae, such as the Type Iax–class prototype SN 2002cx, are described by a variety of models such as the failed detonation and partial deflagration of an accreting carbon-oxygen white dwarf star or the explosion of an accreting, hybrid carbon-oxygen-neon core. These models predict that bound remnants survive such events with, according to some simulations, a high kick velocity. We report the discovery of a high proper motion, low-mass white dwarf (LP 40-365) that travels at a velocity greater than the Galactic escape velocity and whose peculiar atmosphere is dominated by intermediate-mass elements. Strong evidence indicates that this partially burnt remnant was ejected following a subluminous Type Ia supernova event. This supports the viability of single-degenerate supernova progenitors.

Type Ia supernova (SN Ia) explosions are powered by the detonation of a Chandrasekhar-mass white dwarf with a degenerate carbon-oxygen core (*1*). Models show that the explosion may be triggered by the high internal pressure caused either by matter accreted from a close donor star [the single-degenerate (SD) scenario] or by the merger with another white dwarf (the double-degenerate scenario) (*2*). Although Type Ia supernovae are used to calibrate the cosmological distance scale (*1*) and constrain cosmological models (*3*, *4*), our knowledge of these objects is incomplete, and their progenitors have remained elusive (*5*, *6*). The possibility of detecting surviving remnants from subluminous SN Ia events may help illuminate the SN Ia progenitor problem in general. Models (*7*–*9*) proposed to explain observed properties of subluminous SN Ia such as the SN Iax–class prototype SN 2002cx (*10*, *11*) involve failed detonation and partial deflagration of a massive white dwarf (*7*–*9*) or the explosion of a hybrid carbon-oxygen-neon (CONe) core (*12*, *13*), with both scenarios expected, under the right circumstances, to leave a bound remnant. Direct evidence for such remnants is missing (*5*).

We have observed the high proper motion star LP 40-*365* (*14*). An identification spectrum was obtained on 2015 February 21 using the Richtey-Chretien spectrograph attached to the Mayall 4-m telescope at Kitt Peak National Observatory (KPNO) (Fig. 1). The main characteristics are a blue continuum indicating a temperature of ≈10,000 K (circa B9 star); the complete absence of neutral hydrogen or helium absorption lines, unlike in normal B stars; and the appearance of strong magnesium (Mg I and Mg II) and sodium (Na I) line series and weaker lines of oxygen (O I). Table 1 lists astrometric (*15*) and photometric (*16*) data for this object. We followed up this unusual spectrum using low- to high-dispersion spectra obtained between June 2015 and June 2016 with the William Herschel 4.2-m telescope on La Palma, the Hiltner 2.4-m telescope on Kitt Peak, and, finally, with the Gemini-North 8-m telescope on Mauna Kea (*17*).

We performed a spectral line analysis using an iterative procedure that adjusts a parametrized spectral synthesis to the observed line spectrum using χ^2 minimization techniques. These calculations were performed by using a multiparameter fitting procedure that constrains simultaneously the effective temperature ($T_{\rm eff}$) and surface gravity ($\log g$) of the star and each individual element abundance in the atmosphere (*17*). We analyzed the high-resolution spectra obtained with the Echelle SpectroPolarimetric Device for the Observation of Stars (ESPaDOnS) fed by optical fibers attached to the Gemini-North telescope using the Gemini Remote Access to CFHT ESPaDOnS Spectrograph (GRACES) (CFHT, Canada-France-Hawaii Telescope).

The model atmospheres and synthetic spectra supporting our analysis were calculated in full non–local thermodynamic equilibrium (non-LTE) by using the computer codes TLUSTY version 204 and SYNSPEC version 49 (*17*, *18*). The chemical composition includes elements with atomic numbers from Z = 1 (H) to 30 (Zn) with all relevant ionized atoms. The atmosphere is in radiative equilibrium; convective energy transport was found to be inefficient. Detailed line profiles were calculated by using line-broadening parameters dominated by electronic collisions (Stark effect). Table 1 lists best-fitting stellar parameters (with 1σ statistical error bars) and Fig. 2 shows the corresponding abundances. The high $T_{\rm eff}$ and the $\log g$, which is intermediate between normal white dwarfs and the main sequence stars,

Table 1. Stellar data and parameters. The celestial coordinates are provided along the right ascension (RA ≡ α) and declination (Dec ≡ δ) and the apparent motion of the star, i.e., the proper motion μ, is decomposed into $\mu_\alpha \cos\delta$ along the right ascension and μ_δ along the declination.

Parameter	Measurement
RA (J2000)	$14^h06^m35^s.45$
Dec (J2000)	+74°18′58″.0
$\mu_\alpha \cos\delta$	−56 ± 7 mas year^{-1}
μ_δ	148 ± 7 mas year^{-1}
m_V	15.51 ± 0.09 mag
$T_{\rm eff}$	$10,100^{+250}_{-350}$ K
$\log g$/(cm s^{-2})	$5.80^{+0.20}_{-0.35}$
Mass	$0.14\pm0.01 M_\odot$
Radius	$0.078^{+0.040}_{-0.020} R_\odot$
M_V	$8.14^{+0.60}_{-0.90}$ mag
$v \sin i$	30.5 ± 2.0 km s^{-1}

[1]Astronomický ústav, Akademie věd České republiky, Fričova 298, CZ-251 65 Ondřejov, Czech Republic. [2]Dr. Karl Remeis–Sternwarte, Astronomical Institute, University Erlangen-Nürnberg, Sternwartstr. 7, 96049 Bamberg, Germany. [3]Astroserver.org, 8533 Malomsok, Hungary. [4]Department of Physics and Astronomy, 6127 Wilder Laboratory, Dartmouth College, Hanover, NH 03755-3528, USA. [5]Département de physique et d'astronomie, Université de Moncton, Moncton, New Brunswick E1A 3E9, Canada. [6]Mathematical Sciences Institute, The Australian National University, Canberra, ACT 0200, Australia.
*Corresponding author. Email: vennes@asu.cas.cz

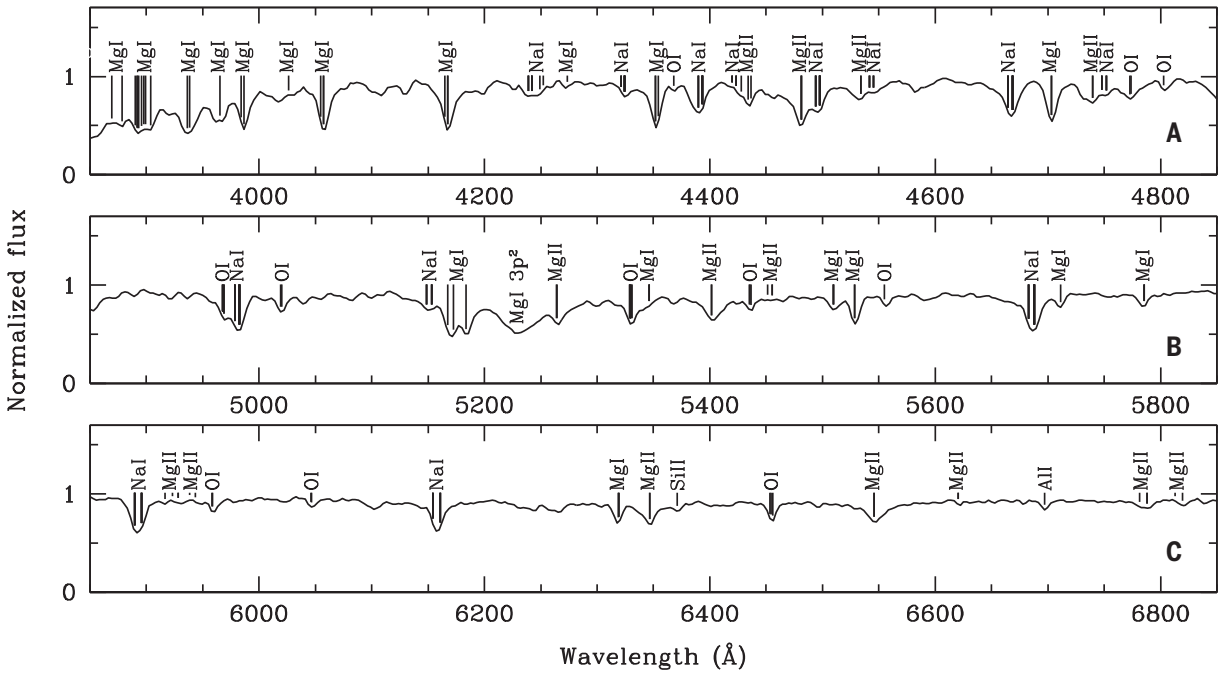

Fig. 1. Normalized optical spectrum of LP 40-365 as a function of wavelength. The spectrum was obtained with the Richey-Chretien Spectrograph at the 4-m telescope (KPNO). Dominant spectral lines of sodium (Na I) and magnesium (Mg I and Mg II) are labeled, along with weaker lines of oxygen (O I), aluminum (Al I) and silicon (Si II). A broad feature near 5230 Å is tentatively identified with a resonance in the Mg I $3p^2$ photoionization cross section.

indicate that this object is most likely a low-mass degenerate star (*19*). The line profiles demonstrate that the star is rotating with a projected rotation velocity $v \sin i = 30.5$ km s^{-1}, where i is the apparent inclination of the rotation axis and v is the equatorial rotation velocity, suggesting that the parent body was spun up during binary interaction. The abundance analysis shows that the main atmospheric constituents are oxygen and neon, with substantial traces of intermediate-mass elements such as aluminum and silicon.

We measured a large Doppler wavelength shift in the spectral line analysis. From a sample of 21 velocity measurements taken at different epochs and after correcting for Earth's motion, we measured an average radial velocity $v_r = 497.6 \pm 1.1$ km s^{-1}, without significant variations ($\chi^2_r = 1.3$). Therefore, the star is apparently single and moving at a velocity characteristic of hypervelocity stars (*20*). Those objects are former members of binary systems that were ejected during three-body encounters with the Galactic center (GC) or ejected following the demise of a massive white dwarf companion in a SD SN Ia (*21*).

In addition to its large radial velocity, LP 40-365 shows a large apparent motion across the celestial sphere of $\mu = 158$ milli–arc sec per year (mas year^{-1}). With knowledge of the distance d, the proper motion vector may be converted into the tangential velocity vector v_T, which, combined with the radial velocity v_r, provides a complete three-dimensional description of LP 40-365's motion. We estimated the distance toward LP 40-365 with a photometric method (*17*), using as inputs the apparent luminosity of the star and an estimate of its absolute lumimosity. The absolute luminosity is calculated by using the surface temperature measurements described earlier and an estimate of the stellar radius, which is model dependent. However, that distance estimate will eventually be superseded by Gaia parallax measurements (*22*).

The radius of a low-mass, degenerate or partly degenerate body is sensitive to finite-temperature effects (*23*, *24*) that would inflate the radius of a young, extremely low-mass white dwarf such as LP 40-365. Models for carbon, oxygen, silicon, or iron cores are available (*25*), but unfortunately, the predicted surface gravity of available models ($\log g > 6.0$, where g is expressed in cm s^{-2}) largely exceeds the measured gravity of LP 40-365, indicating that its mass should be much lower than 0.3 solar mass ($M_\odot$). Lower-mass models with helium interiors are available (*23*) and indicate that a body with a mass of $\approx 0.14\,M_\odot$ and ≈8% of the solar radius ($R_\odot$) reproduces the log g and T_{eff} of LP 40-365, assuming a cooling age between 5 and 50 million years (*17*). Although we have concluded that the interior of LP 40-365 is most likely composed of carbon, oxygen, and neon, or heavier elements, helium models characterized by identical mean electronic weight ($\mu_e = 2$) represent a reasonable proxy. The central temperature of the adopted model, $T_c \approx 30 \times 10^6$ K, is lower than that of a typical inert core of normal white dwarfs (*23*). Adopting a radius of $0.078\,R_\odot$, we estimated an absolute magnitude in the Johnson V band $M_V = 8.14$ magnitude (mag). Thus, the apparent M_V magnitude listed in Table 1 implies a distance of 298^{+150}_{-70} pc. The tangential velocity at a distance of 298 pc is v_T = 224 km s^{-1}, for a total space velocity relative to the Sun of 546 km s^{-1}.

To retrace the past history of this object, we converted the apparent velocity components (radial and tangential) into the Galactic velocity vector (*26*) (*U*, *V*, *W*) = (–346, 360, 217) km s^{-1}. This instantaneous velocity vector may be projected back in time by adopting an appropriate Galactic potential model (*27*). We followed the Galactic orbit of LP 40-365 from the present time ($t = 0$) back to $t = -100$ million years. The projected trajectories displayed in Fig. 3 indicate that, for an assumed starting point set at distances between 100 and 1000 pc, the object did not encounter the GC and, therefore, is not the product of a three-body dynamical interaction with the GC (*28*). None of the resultant trajectories, which allowed for uncertainties in the distance, are bound Galactic orbits either. The total velocity in the Galactic rest frame varies between 675 km s^{-1}, assuming $d = 100$ pc, and 1016 km s^{-1}, assuming $d = 1000$ pc, with a velocity of 709 km s^{-1} at the distance (298 pc) set by the photometric method. All exceed the Galactic escape velocity at 8.5 kpc from the GC (*20*). The object must have originated along one of those projected trajectories, and the trajectory that took LP 40-365 to the present-day distance of 298 pc entered the plane <5 million years ago. The simulated cooling time scale for a $0.15\,M_\odot$ compact object with an T_{eff} of 10^4 K is only ≈5 to 50 million years (*23*).

Combining the peculiar surface composition of this compact object, the results of the trajectory analysis, and the evolutionary age estimate, it appears likely that LP 40-365 is the surviving

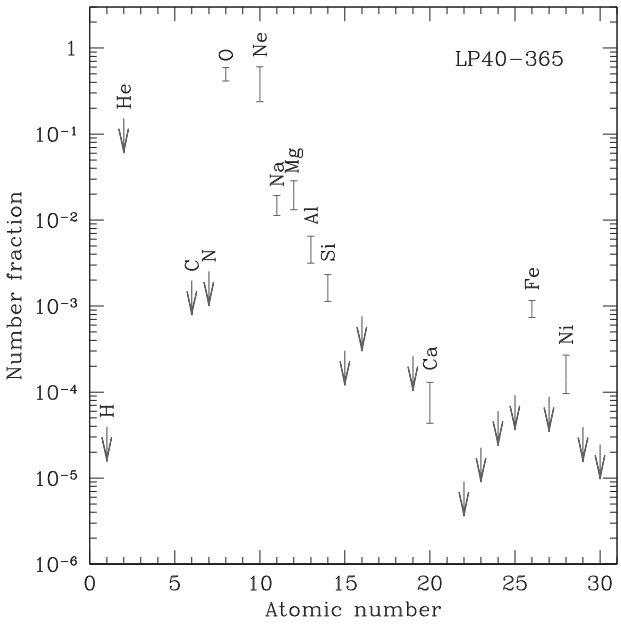

Fig. 2. Elemental abundances for LP 40-365. Photospheric abundances, expressed as the number fraction versus the atomic number, were measured in the high-dispersion spectrum obtained with GRACES at the Gemini-North telescope on Mauna Kea. The atmosphere is dominated by oxygen and neon, followed by sodium and magnesium. Iron is more abundant than nickel and other elements in the iron group by at least a factor of 10. Upper limits are shown with arrows.

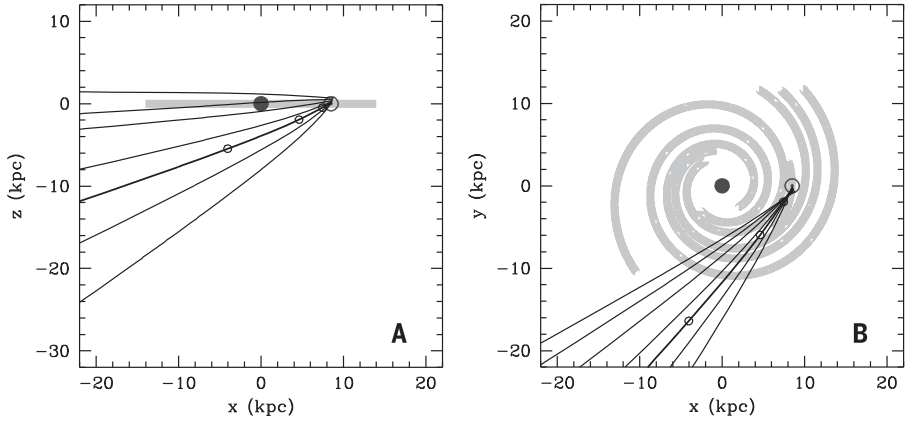

Fig. 3. Calculated Galactic motion of LP 40-365. The orbits are drawn (**A**) in the Galactic plane (*z* versus *x*) and (**B**) perpendicular to the plane (*y* versus *x*) with the GC (solid circle) at the origin. The Sun (⊙) is located 8.5 kpc along the *x* axis. The current (t = 0) position of LP 40-365 is estimated assuming a distance to the Sun of, from uppermost to lowermost curve, 1000, 800, 600, 400, 300, 200, and 100 pc. The past trajectory resulting from an assumed distance of 300 pc is marked with open circles at, from rightmost to leftmost curve, −3, −10, and −30 million years. Schematic views of the Galactic arms are shown in gray.

remnant of a subluminous SN Ia event that took place below the Galactic plane, a few kiloparsecs away and earlier than 50 million years ago. The stellar properties and the kinematics of LP 40-365 are comparable to some simulated events (*7*), suggesting that this object is indeed a fragment that survived the failed detonation of an SN Iax. The mass estimate is somewhat less than accounted for in these simulations (>0.3 $M_{\odot}$). However, other models (*9*) successfully achieve remnants with masses as low as 0.09 $M_{\odot}$ but without delivering a large kick velocity. Variations in the adopted ignition geometry, such as centered versus off-center ignition, may affect the kinematical outcome for the surviving remnant. Simulations involving hybrid CONe cores (*13*) successfully generated low-mass remnants, but these simulations did not explore postexplosion kinematics.

Intermediate-mass elements detected in the atmosphere of LP 40-365 are expected to contaminate bound remnants after a typical SN Iax event (*9*), but we found only minute traces of iron-group elements, which normally dominate the supernova ejecta. The paucity of iron-group elements and the prevalence of lighter elements indicate that gravitational settling and chemical separation may have occurred with light elements dominating over heavier ones. It is not possible to estimate the fraction of iron material produced in the explosion that would manage to diffuse to the star's center. Diffusion time scales at the star's surface may be comparable to or longer than the age of the object (*29*). Conversely, the absence of carbon and prevalence of oxygen and neon at the surface of LP 40-365 would preferably match the configuration of a hybrid CONe core (*13*). None of the simulations take element diffusion explicitly into account; therefore, a detailed comparison of predicted and observed surface compositions would not constitute a definitive test for any models.

It has been suggested that dynamical instability in a low-mass x-ray binary orbiting a distant main sequence star could result in the high-velocity ejection of the donor star (*30*, *31*). Apart from an unspecified surface composition, the predicted high-velocity star could resemble LP 40-365. However, only ~10^{-8} such events are expected per year in the Milky Way (*31*), compared to a rate of ~10^{-3} for SN Iax events (*32*); therefore, this scenario is less probable.

The actual donor star that must also have been ejected (*21*) along with LP 40-365 should be detectable as well. For example, the high-velocity, helium-rich subdwarf star US 708 (*33*) is a representative of the class of donor stars that emerged from a SD SN Ia event, and a similar object would have been ejected along with LP 40-365 after the proposed underluminous SN Ia event. The possible detection of a bound remnant in the aftermath of the SN Iax event SN 2008ha has been reported, although it may be a chance alignment (*32*). The properties of that object are unknown. The tentative progenitor of SN 2012Z has been described as novalike (*34*), suggesting the likely presence of an accreting white dwarf in a SD progenitor system akin to that of LP 40-365. No bound remnant has been identified. The atmospheric properties of LP 40-365 share some similarities with those of another extreme white dwarf (*35*) but exhibit clear distinctions as well: Both WD 1238+674 and LP 40-365 are oxygen rich, but WD 1238+674 is more massive (0.6 $M_{\odot}$ versus 0.14 $M_{\odot}$) and its kinematical properties do not appear as extreme. The discovery of the oxygen-neon white dwarf WD 1238+674 lends support to the hybrid CONe formation model (*36*) and, indirectly, to the subluminous SN Ia explosion models involving hybrid CONe white dwarfs (*13*).

REFERENCES AND NOTES

1. K. Nomoto, K. Iwamoto, N. Kishimoto, *Science* **276**, 1378–1382 (1997).
2. I. Iben Jr., A. V. Tutukov, *Astrophys. J. Suppl. Ser.* **54**, 335–372 (1984).
3. A. G. Riess *et al.*, *Astron. J.* **116**, 1009–1038 (1998).
4. S. Perlmutter *et al.*, *Astrophys. J.* **517**, 565–586 (1999).
5. D. Maoz, F. Mannucci, G. Nelemans, *Annu. Rev. Astron. Astrophys.* **52**, 107–170 (2014).
6. B. Wang, Z. Han, *New Astron. Rev.* **56**, 122–141 (2012).
7. G. C. Jordan IV, H. B. Perets, R. T. Fisher, D. R. van Rossum, *Astrophys. J.* **761**, L23 (2012).
8. M. Kromer *et al.*, *Mon. Not. R. Astron. Soc.* **429**, 2287–2297 (2013).
9. M. Fink *et al.*, *Mon. Not. R. Astron. Soc.* **438**, 1762–1783 (2014).
10. D. Branch *et al.*, *Publ. Astron. Soc. Pac.* **116**, 903–908 (2004).
11. R. J. Foley *et al.*, *Astrophys. J.* **767**, 57 (2013).
12. M. Kromer *et al.*, *Mon. Not. R. Astron. Soc.* **450**, 3045–3053 (2015).
13. E. Bravo, P. Gil-Pons, J. L. Gutiérrez, C. L. Doherty, *Astron. Astrophys.* **589**, A38 (2016).
14. W. J. Luyten, *Proper Motion Survey with the 48-inch Schmidt Telescope. XXII. Special Catalogues for the Zone +70deg to +75deg* (Univ. of Minnesota Press, 1970).

15. S. Lépine, M. M. Shara, *Astron. J.* **129**, 1483–1522 (2005).
16. C. Watson, A. A. Henden, A. Price, *VizieR Online Data Catalog: AAVSO International Variable Star Index VSX (Watson+, 2006-2014)* (Smithsonian Astrophysical Observatory/NASA Astrophysics Data System, 2016).
17. Materials and methods are available as supplementary materials.
18. I. Hubeny, T. Lanz, *Astrophys. J.* **439**, 875–904 (1995).
19. S. Gianninas *et al.*, *Astrophys. J.* **794**, 35 (2014).
20. W. R. Brown, *Annu. Rev. Astron. Astrophys.* **53**, 15–49 (2015).
21. S. Justham, C. Wolf, P. Podsiadlowski, Z. Han, *Astron. Astrophys.* **493**, 1081–1091 (2009).
22. M. A. C. Perryman *et al.*, *Astron. Astrophys.* **369**, 339–363 (2001).
23. L. G. Althaus, O. G. Benvenuto, *Astrophys. J.* **477**, 313–334 (1997).
24. O. G. Benvenuto, L. G. Althaus, *Mon. Not. R. Astron. Soc.* **303**, 30–38 (1999).
25. J. A. Panei, L. G. Althaus, O. G. Benvenuto, *Astron. Astrophys.* **353**, 970–977 (2000).
26. D. R. H. Johnson, D. R. Soderblom, *Astron. J.* **93**, 864–867 (1987).
27. C. Allen, A. Santillan, *Rev. Mex. Astron. Astrofis.* **22**, 255–263 (1991).
28. J. G. Hills, *Nature* **331**, 687–689 (1988).
29. C. Paquette, C. Pelletier, G. Fontaine, G. Michaud, *Astrophys. J. Suppl. Ser.* **61**, 197–217 (1986).
30. P. C. C. Freire *et al.*, *Mon. Not. R. Astron. Soc.* **412**, 2763–2780 (2011).
31. S. Portegies Zwart, E. P. J. van den Heuvel, J. van Leeuwen, G. Nelemans, *Astrophys. J.* **734**, 55 (2011).
32. R. J. Foley *et al.*, *Astrophys. J.* **792**, 29 (2014).
33. S. Geier *et al.*, *Science* **347**, 1126–1128 (2015).
34. C. McCully *et al.*, *Nature* **512**, 54–56 (2014).
35. S. O. Kepler, D. Koester, G. Ourique, *Science* **352**, 67–69 (2016).
36. C. L. Doherty, P. Gil-Pons, L. Siess, J. C. Lattanzio, H. H. B. Lau, *Mon. Not. R. Astron. Soc.* **446**, 2599–2612 (2015).

ACKNOWLEDGMENTS

A.K. and S.V. acknowledge support from the Grant Agency of the Czech Republic (15-15943S). A.K. was a visiting astronomer at KPNO, National Optical Astronomy Observatory. This work was also supported by the project RVO:67985815 in the Czech Republic. The research leading to these results has received funding from the European Community's Seventh Framework Programme (FP7/2013-2016) under grant agreement number 312430 [Optical Infrared Coordination Network for Astronomy (OPTICON)]. J.R.T. acknowledges support from NSF grant AST-1008217. This research made use of services at Astroserver.org under the reference number NWKZKA and is based on observations obtained at KPNO, National Optical Astronomy Observatory, and at the Gemini Observatory, program GN-2016A-FT-24, using ESPaDOnS, located at the CFHT. This publication makes use of data products from the Wide-field Infrared Survey Explorer, the Two Micron All-Sky Survey, and the American Association of Variable Sky Observers (AAVSO) Photometric All-Sky Survey (APASS). Complete acknowledgments are included in the supplementary material. Observational data are available in publicly available archives, as are our calculated model atmospheres. Full details and URLs are given in the supplementary material.

SUPPLEMENTARY MATERIALS

www.sciencemag.org/content/357/6352/680/suppl/DC1
Materials and Methods
Supplementary Text
Figs. S1 to S8
Tables S1 and S2
References (*37*–*58*)

23 January 2017; accepted 18 July 2017
10.1126/science.aam8378

BROWN DWARFS

Zones, spots, and planetary-scale waves beating in brown dwarf atmospheres

D. Apai,[1,2]* T. Karalidi,[1] M. S. Marley,[3] H. Yang,[1] D. Flateau,[1,4] S. Metchev,[5,6] N. B. Cowan,[7,8,9] E. Buenzli,[10] A. J. Burgasser,[11] J. Radigan,[12] E. Artigau,[9] P. Lowrance[13]

Brown dwarfs are massive analogs of extrasolar giant planets and may host types of atmospheric circulation not seen in the solar system. We analyzed a long-term Spitzer Space Telescope infrared monitoring campaign of brown dwarfs to constrain cloud cover variations over a total of 192 rotations. The infrared brightness evolution is dominated by beat patterns caused by planetary-scale wave pairs and by a small number of bright spots. The beating waves have similar amplitudes but slightly different apparent periods because of differing velocities or directions. The power spectrum of intermediate-temperature brown dwarfs resembles that of Neptune, indicating the presence of zonal temperature and wind speed variations. Our findings explain three previously puzzling behaviors seen in brown dwarf brightness variations.

Brown dwarfs are substellar and super-planetary in mass, but in size, temperature, composition, and chemistry, they are analogous to gas giant exoplanets (*1*). Isolated brown dwarfs are easier to study than exoplanets, making them valuable laboratories for investigating low-temperature (250 to 2000 K) atmosphere models. This includes the structure and dynamics of atmospheres, traced through observations of rotationally modulated variability and variations in spectral line profile shapes. Models of brown dwarf atmospheric dynamics predict two different types of circulation: a stable zonal pattern (rotationally dominated case) and stochastic, unstructured circulation (heat transport–dominated case) (*2*).

Heterogeneous condensate clouds (such as silicates) have recently been detected in brown dwarfs (*3*–*5*), offering tracers of the previously inaccessible atmospheric circulation of these objects. High-precision, time-resolved infrared observations sample the rotational phase dependence of disk-integrated emission, probing the distribution of clouds in a modest number of brown dwarfs (*5*, *6*). Rotational phase mapping studies have found that most if not all brown dwarfs have heterogeneous cloud cover (*7*, *8*); that the highest-amplitude rotational modulations in the 1- to 2.5-μm atmospheric windows are seen among objects at the transition between the silicate cloud-dominated L-type and the cooler (≲1300 K) T-types (*9*); and that the variability of L/T transition brown dwarfs is caused by simultaneous cloud thickness and brightness temperature variations (*3*–*6*, *10*). Brown dwarf lightcurves often display pressure-dependent phase shifts, revealing relatively complex longitudinal-vertical structures (*11*–*13*). Some brown dwarfs' lightcurves evolve in time (*3*, *12*, *14*, *15*), indicating vigorous atmospheric dynamics.

Despite this improving understanding, three types of prominent behavior remain confusing: (i) single-peaked (one peak per rotation) lightcurves splitting into double-peaked lightcurves (*4*, *12*); (ii) rapid transitions from very low-amplitude lightcurves (<0.5%) to high-amplitude ones (~5%) (*12*); and (iii) an apparently recurring feature in an otherwise irregularly evolving lightcurve (*15*). Atmospheric models based on elliptical spots (akin to the Great Red Spot on Jupiter) have been proposed to match or approximate lightcurve segments (typically a single rotation) (*3*, *5*, *15*), but no physically viable model has yet been proposed to explain the dramatic lightcurve evolution seen over a time scale of a few rotational periods.

We monitored a sample of ultracool brown dwarfs over 1.5 years, covering approximately 192 complete brown dwarf rotations (Fig. 1 and figs. S8 to S13). Our data sample atmospheric evolution over baselines up to 1000 rotations. The targets were brown dwarfs with known rotational modulations and with a range of temperature (800 to ~1500 K) and rotational periods (1.4 to 13 hours) (*16*). We observed each brown dwarf at eight epochs, each covering four complete rotations: Spitzer Channel 1 [central wavelength

[1]Steward Observatory, The University of Arizona, 933 N. Cherry Avenue, Tucson, AZ 85721, USA. [2]Lunar and Planetary Laboratory, University of Arizona, 1640 E. University Boulevard, Tucson, AZ 85721, USA. [3]NASA Ames Research Center, Moffett Field, CA 94035, USA. [4]Department of Physics, University of Cincinnati, 2600 Clifton Avenue, Cincinnati, OH 45221, USA. [5]Department of Physics and Astronomy and Centre for Planetary Science and Exploration, University of Western Ontario, London, ON N6A 3K7, Canada. [6]Department of Physics and Astronomy, Stony Brook University, Stony Brook, NY 11795-3800, USA. [7]Department of Earth and Planetary Sciences, McGill University, 3450 Rue University, Montreal, QC H3A 2A7, Canada. [8]McGill Space Institute, 3550 Rue University, Montréal, QC H3A 2A7, Canada. [9]Institut de Recherche sur les Exoplanètes (IREx), Département de Physique, Université de Montréal, C.P. 6128, Succ. Centre-Ville, Montréal, QC H3C 3J7, Canada. [10]Institute for Astronomy, ETH Zürich Wolfgang-Pauli-Straße 27, 8093 Zürich, Switzerland. [11]Center for Astrophysics and Space Science, University of California, San Diego, La Jolla, CA 92093, USA. [12]Department of Physics, Utah Valley University, 800 West University Parkway, Orem, UT 84058, USA. [13]Infrared Processing and Analysis Center, MS 314-5, California Institute of Technology, 1200 E. California Boulevard, Pasadena, CA 91125, USA.
***Corresponding author. Email: apai@arizona.edu**